Enhancing the thermoelectric performance of n-type Mg_3Sb_2-based materials via Ag doping

Jiankang Li[1,2], Raju Chetty[1], Zihang Liu[1], Weihong Gao[1] and Takao Mori[1,2 *]*

[1]*Research Center for Materials Nanoarchitectonics (MANA), National Institute for Materials Science (NIMS), Namiki 1-1, Tsukuba 305-0044, Japan*

[2]*Graduate School of Pure and Applied Sciences, University of Tsukuba, Tennodai 1-1-1, Tsukuba 305–8671, Japan*

E-mail: CHETTY.Raju@nims.go.jp, MORI.Takao@nims.go.jp

Keywords: Thermoelectric, Zintl compound, Mg_3Sb_2, Ag doping

Abstract

The n-type $Mg_3(Sb, Bi)_2$ alloys show great potential for wasted heat energy harvesting due to their promising thermoelectric properties. In this work, we discover that doping transition element Ag into the n-type $Mg_3(Sb, Bi)_2$ alloy can effectively optimize the power factor and suppress the lattice thermal conductivity simultaneously. Interestingly, the Ag doping has different effects compared to the isoelectronic and same group element Cu addition studied previously. A high power factor of 19.6 $\mu Wcm^{-1}K^{-2}$ is obtained at 673 K owing to the increased electrical conductivity. At the same time, the lattice thermal conductivity is reduced to ~0.5 $Wm^{-1}K^{-1}$ because of enhanced phonon scattering induced by Ag atoms. These improvements lead to a peak figure of merit (*ZT*) of 1.64 at 673 K as well as a high average *ZT* of 1.27 is obtained from 323 K to 673 K. Furthermore, a thermoelectric single leg with a competitive conversion efficiency of ~11% under a hot-side temperature of 673 K is fabricated successfully. In addition, a 2-pair module composed of n-type $Mg_3(Sb, Bi)_2$ alloy and p-type MgAgSb-based compound demonstrates the high conversion efficiency of ~7.9% at a temperature difference of 277 K, which will significantly upgrade the sustainable energy recycling technology.

1. Introduction

Thermoelectric (TE) materials offer great prospects for energy harvesting as they can directly convert thermal energy into electric energy and offer a promising solution for powering Internet of Things (IoT)[1–3]. It is crucial to develop high-performance TE materials to fully harness their capabilities. The efficiency of TE materials can be evaluated by the dimensionless figure of merit, given by the equation, $ZT = S^2\sigma T/(\kappa_L+\kappa_e)$. Here, S is the Seebeck coefficient, σ is the electrical conductivity, κ_L is the lattice thermal conductivity, κ_e is the electronic thermal conductivity, and T is the absolute temperature[4]. A higher ZT value normally means a more efficient TE material. However, optimizing the ZT value is challenging because the various parameters are interdependent. Simply adjusting one parameter without considering the others may not yield the desired outcome, therefore, achieving optimal ZT values requires a comprehensive approach that takes into account the interplay relationship among these parameters. Many strategies have been adopted to enhance ZT, such as band engineering[5–7], point defect engineering[8,9], microstructure modification[10,11] and carrier concentration optimization[12,13].

So far, the most mature TE material is Bi_2Te_3-based alloys, which have already realized commercialization in salient cooling applications and heat recycling[14]. However, the scarcity of Te restrains its further development. Many novel TE systems have already been explored aiming to challenge or even replace the supremacy of Bi_2Te_3-based materials in this field, such as $AgSbTe_2$[15,16], GeTe[17,18], $CoSb_3$[19], Zintl compounds, etc. Among those novel TE material systems, Zintl compounds, with complex structures and rich crystal chemistry are close to the concept of 'PGEC', which is 'phonon glass-electron crystal'[20]. Mg_3Sb_2, owing to low raw material price, and less toxicity, is a promising Zintl compound and shows high potential in future TE module applications[21,22]. Due to the high volatility of Mg, Mg_3Sb_2 has been acknowledged as a p-type TE material with a mediocre performance at first, which strongly limits its further development[23–25].

In 2016, Tamaki *et al.*[26] demonstrated the n-type transport of Mg_3Sb_2-based TE material by adding excess Mg to suppress its evaporation during sintering. The highest ZT ~1.5 is obtained at 723 K in

sample $Mg_{3.2}Sb_{1.5}Bi_{0.49}Te_{0.01}$, realizing a great leap forward in the enhancement of n-type Mg_3Sb_2-based material. Motivated by this, many transition elements have already been proven as suitable dopants for n-type Mg_3Sb_2. For example, Chen *et al*.[27] adopted Mn as a dopant into the Mg site to change the low-temperature carrier scattering mechanism and enhance carrier mobility. Liu *et al*.[10] demonstrated that introducing minor Cu into interstitial sites is an applicable strategy for optimizing power factor ($PF = S^2\sigma$) and κ_L together. Despite these significant reports, transition element-doped Mg_3Sb_2-based TE materials are less investigated and need more exploration. For example, Ag, which is in the same group as Cu in the periodic table of elements (IB), has been proven as an effective dopant for the p-type Mg_3Sb_2 system[24,28]. Despite its potential, Ag doping in n-type systems remains unexplored, which motivates our interest in investigating its effects.

In this work, the effect of Ag doping on the TE performance of n-type $Mg_{3.2}Sb_{1.5}Bi_{0.49}Te_{0.01}$ was studied. High-density n-type $Mg_{3.2}Ag_xSb_{1.5}Bi_{0.49}Te_{0.01}$ (x = 0, 0.005, 0.01, and 0.02) disks were prepared by the one-step ball milling and spark plasma sintering method. We found that Ag doping can effectively increase σ by the improvement of mobility. Also, thanks to the almost unchanged Seebeck coefficient after Ag doping, PF was improved from 16.7 to 19.6 μW cm^{-1} K^{-2} at 673 K. At the same time, Ag partially goes into the Mg sites to enhance the phonon scattering, realizing a decrease in lattice thermal conductivity. Consequently, the highest ZT ~1.64 was achieved at 673 K, and ZT also reached 0.72 at 323 K, showing a high TE performance over the whole measuring range. Furthermore, a 2-pair TE module using the corresponding material as n-type legs and MgAgSb as p-type legs was fabricated and the maximum conversion efficiency reached ~7.9% at a heat source of 573 K, which is comparable to the published results and also competitive in other module systems.

2. Results and discussion

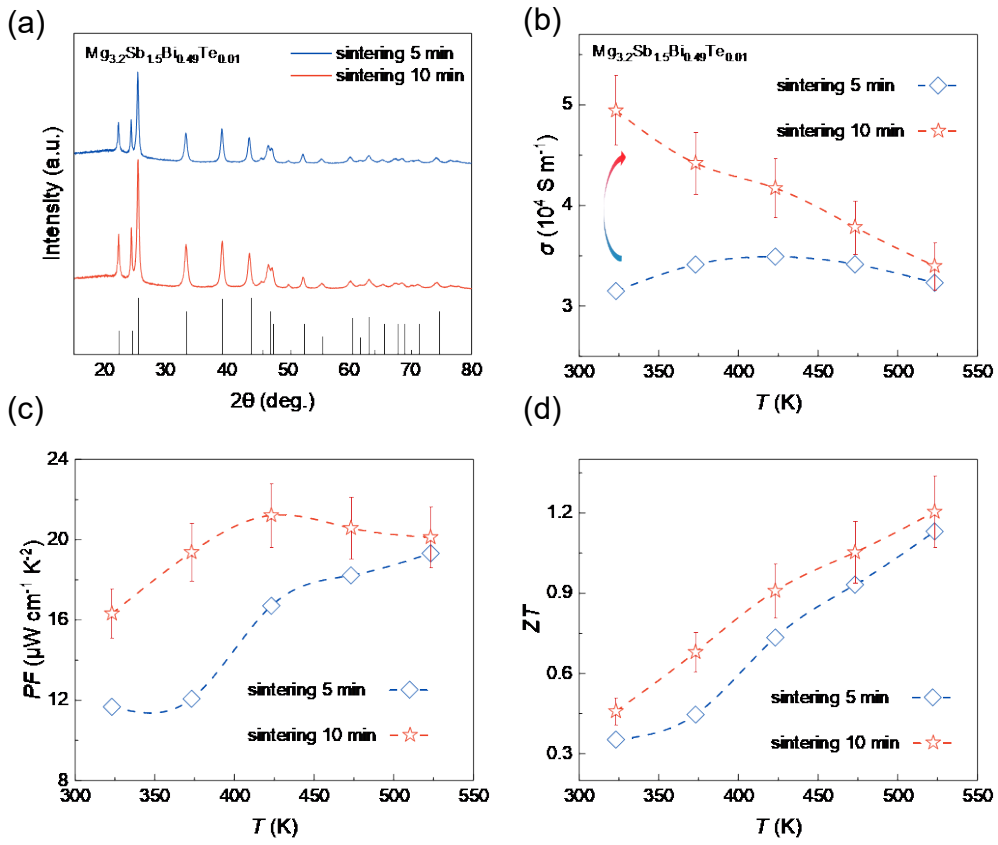

Figure 1. (a) X-ray diffraction pattern of $Mg_{3.2}Sb_{1.5}Bi_{0.49}Te_{0.01}$ with 5 minutes and 10 minutes sintering. (b-d) Temperature-dependent (b) σ, (c) *PF*, (d) *ZT* of $Mg_{3.2}Sb_{1.5}Bi_{0.49}Te_{0.01}$ with 5-minute sintering and 10-minute sintering.

Mg_3Sb_2-based TE material system usually has a low TE performance at low-temperature range. To solve this problem, one common strategy is to shift the $Mg_3(Sb, Bi)_2$ from Sb-rich to Bi-rich[29]. However, the low thermal and chemical stability of Mg_3Bi_2-based materials is a serious concern [30,31]. In this work, we studied the influence of spark plasma sintering (SPS) time on the TE performance of Sb-rich Mg_3Sb_2 samples. By optimizing the sintering time from 5 minutes to 10 minutes at 973 K, electron scattering was significantly suppressed by eliminating thermal grain-boundary resistance, and therefore electrical performance near room temperature was improved[32]. Figure 1a shows the XRD patterns of $Mg_{3.2}Sb_{1.5}Bi_{0.49}Te_{0.01}$ samples sintered for 5 and 10 minutes. The 10-minute sample has a relatively sharp peak, hinting that sample crystallinity is different[33]. To elucidate this, the scanning electron microscopy (SEM) analysis of fresh fracture surfaces was conducted to check the grain size variation between 5-minute and 10-minute sintered samples (Figure S1). The 10-minute sample exhibits a bigger grain size than the sample sintered at 5 minutes.

In Figure 1b, the σ of the 10-minute sample is elevated to 4.9×10^4 S m^{-1} at 323 K, showing a 57% improvement compared with the 5-minute sample. The almost unchanged S in Figure S2 suggests that the Fermi level of the sample is unchanged, and the raising of σ can be attributed to the reduction of detrimental grain boundary scattering[34]. Consequently, the PF increased from 11.6 μW cm^{-1} K^{-2} to 16.3 μW cm^{-1} K^{-2} at 323 K (Figure 1c). Also, a slightly reduced lattice thermal conductivity κ_L at low temperatures compensates for the increase of elevated electronic thermal conductivity $\kappa_{e,}$, contributing to the slightly increased total thermal conductivity κ and the remarkable enhancement of ZT at low temperatures (Figure S2). Interestingly, reducing the κ_L of material through nano-structuring to create smaller grain sizes is one of the most common strategies to improve TE materials, which should have led the 10-minute sample to show a higher κ_L. While our 10-minute sample shows a lower κ_L although the grain size enlarged, this unphysical grain size dependence of κ_L can be ascribed to the segregation of heavier Bi atoms will increase the lattice thermal resistance at grain boundaries with the increasing sintering time, thus contributing to the degree of inhomogeneity. This unphysical phonon-grain boundary scattering mechanism especially happened on the Sb = 1.5, Bi = 0.49 system[35]. As a result, the ZT increased from 0.35 to 0.45 at 323 K, almost realizing a 30% improvement (Figure 1d). However, no significant improvement in the TE performance was realized for both samples at high temperatures. This is due to the negligible influence of grain size on TE performance at temperatures over 500 K. To improve the TE performance at higher temperatures, Ag was doped into the pristine sample as a strategy.

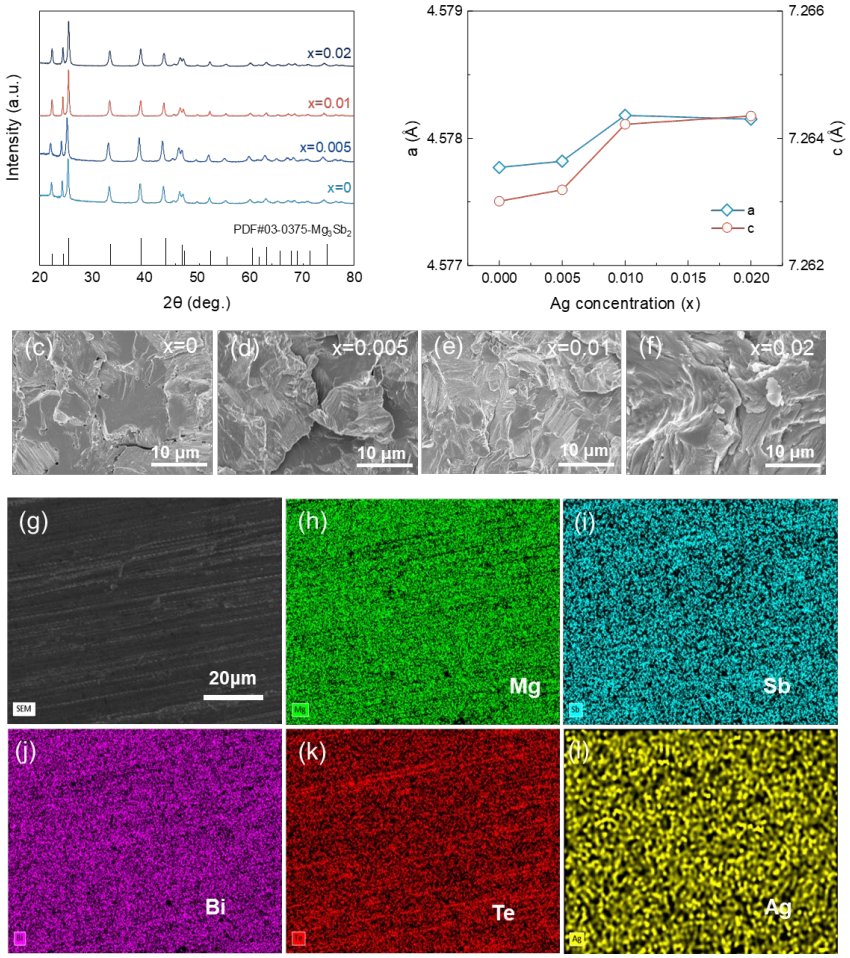

Figure 2. (a) X-ray diffraction pattern, (b) The calculated lattice parameters a and c of the $Mg_{3.2}Ag_xSb_{1.5}Bi_{0.49}Te_{0.01}$ (x = 0, 0.005, 0.01, and 0.02), (c)-(f) SEM image of the fresh cross-section of $Mg_{3.2}Ag_xSb_{1.5}Bi_{0.49}Te_{0.01}$ (x = 0, 0.005, 0.01, and 0.02), respectively. (g-l) EDS element mapping results of $Mg_{3.2}Ag_{0.01}Sb_{1.5}Bi_{0.49}Te_{0.01}$.

The crystal structure of $Mg_{3.2}Ag_xSb_{1.5}Bi_{0.49}Te_{0.01}$ (x = 0, 0.005, 0.01, and 0.02) is the inverse α-La_2O_3 structure (space group *P-3m1*). Figure 2a shows the powder x-ray diffraction (XRD) of $Mg_{3.2}Ag_xSb_{1.5}Bi_{0.49}Te_{0.01}$ (x = 0, 0.005, 0.01, and 0.02) bulk pellets after Spark Plasma Sintering. No secondary phases are found within the detection limits of powder XRD. The lattice parameters *a* and *c* are obtained from the Rietveld refinement of powder XRD of $Mg_{3.2}Ag_xSb_{1.5}Bi_{0.49}Te_{0.01}$ (x = 0, 0.005, 0.01, and 0.02) (Figure S3). The minor addition of Ag increases the lattice parameters slightly as shown in Figure 2b. The reason for the slight increase in both *a* and *c* might be attributed to the partial substitution of Ag on the Mg sites and/or interstitial sites.

Figure 2c-f shows the scanning electron microscopy (SEM) images of fractured surfaces of the $Mg_{3.2}Ag_xSb_{1.5}Bi_{0.49}Te_{0.01}$ (x = 0, 0.005, 0.01, and 0.02) samples. No significant variation in the microstructure is found in all the samples. However, nanopores reduction which is left by the Mg evaporation during the sintering process is observed in all the Ag-added samples, which indicates the suppression of Mg evaporation. Further, an elemental mapping for all the samples is performed by energy dispersive spectroscopy (EDS) as shown in Figure 2g-l. The elemental composition analysis revealed that the Mg content is relatively increased for the Ag-added samples as compared to the pristine compound (Table S1). This result further proves that Ag can restrain the evaporation of Mg during the sintering process [10]. Also, the status of the die and graphite paper was recorded after the sintering process. As shown in Figure S4, the circular graphite paper of the pristine sample looks dirty and the squeezed melting phase is observed simultaneously, which should be ascribed to the Mg evaporation during the sintering[36]. However, the graphite paper of $Mg_{3.2}Ag_{0.01}Sb_{1.5}Bi_{0.49}Te_{0.01}$ looks cleaner than that of the pristine sample, which indicates that Mg evaporation during sintering is well-suppressed by Ag doping. For sample $Mg_{3.2}Ag_{0.07}Sb_{1.5}Bi_{0.49}Te_{0.01}$, completely clean graphite paper proves that more Ag doping can guarantee almost no evaporation of Mg during sintering (As the TE performance of $Mg_{3.2}Ag_{0.07}Sb_{1.5}Bi_{0.49}Te_{0.01}$ is too low which will not be further discussed in this work). This should be attributed to the reaction of Mg and Ag occurring during the sintering at 973 K according to the Ag-Mg binary phase diagram[37].

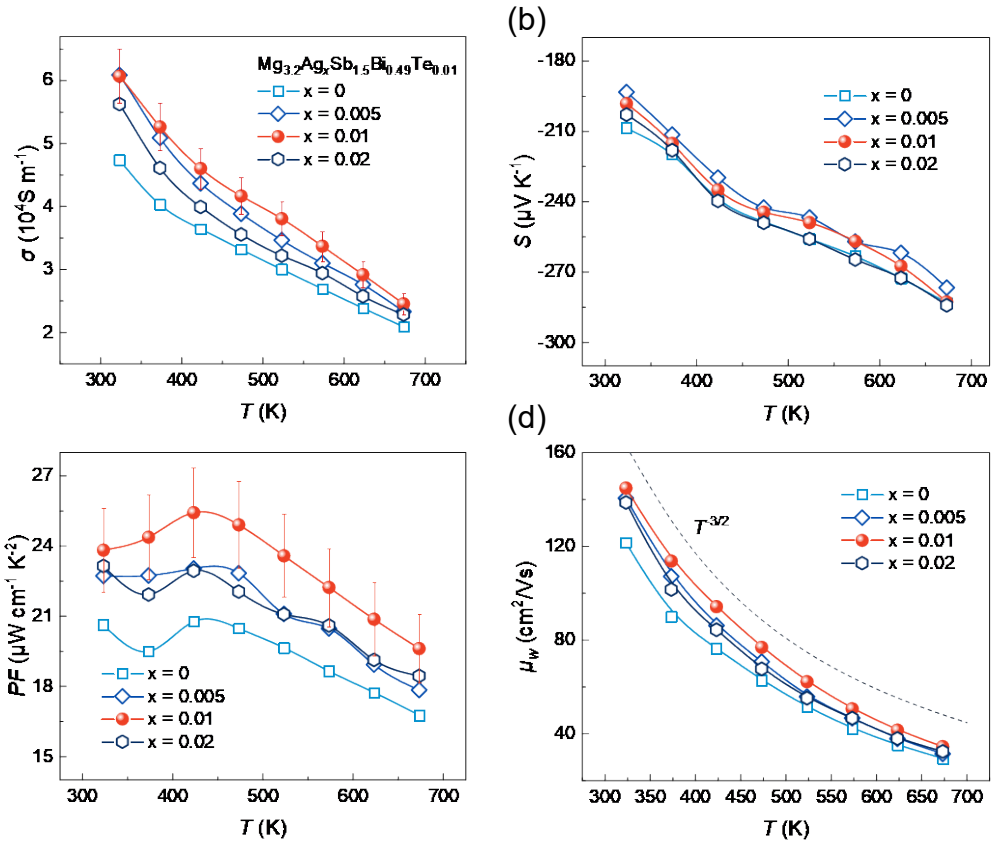

Figure 3. (a-d) Temperature-dependent (a) σ, (b) S, (c) μ_w, (d) PF of $Mg_{3.2}Ag_xSb_{1.5}Bi_{0.49}Te_{0.01}$ (x = 0, 0.005, 0.01, and 0.02).

Temperature dependence of σ for $Mg_{3.2}Ag_xSb_{1.5}Bi_{0.49}Te_{0.01}$ (x = 0, 0.005, 0.01, and 0.02) samples are shown in Figure 3a. The σ of all the samples decreases with the increase of temperature from 323 K to 673 K, which indicates a degenerate semiconducting behavior. This temperature-dependent σ is derived from the acoustic phonon scattering that increases with temperature[33]. Moreover, thermally activated σ is eliminated successfully in the low-temperature range (~323 K) by extending the sintering time[33,34,38], leading all samples to show excellent electrical performance at the low-temperature range. All the doped samples exhibit a higher σ than the pristine sample which proves that Ag doping can effectively optimize the carrier concentration or mobility. The σ at 323 K lifts from 4.7×10^4 S m^{-1} to 6.1×10^4 S m^{-1} by 0.01 Ag doped into the matrix. At 673 K, it reaches 2.45×10^4 S m^{-1} compared with 2.09×10^4 S m^{-1} for the pristine sample. Figure 3b shows the temperature-dependent S and the negative value of the S indicates this compound is an n-type TE material. It is confirmed that the formation of Mg vacancies can be well suppressed by adding the excess Mg grains during the experiment. The value of S displays a noteworthy rise throughout the whole

measured temperature range. However, the *S* of doped samples does not show obvious variation with the pristine sample. An improvement of PF is realized due to the enhanced σ and moderate *S*. As shown in Figure 3c, for $Mg_{3.2}Ag_{0.01}Sb_{1.5}Bi_{0.49}Te_{0.01}$, the highest *PF* reaches 25.4 μW cm^{-1} K^{-2} at 423K and even at 673 K, the *PF* also displays 19.6 μW cm^{-1} K^{-2} in contrast with pristine sample, which is 20.8 μW cm^{-1} K^{-2} at 423 K and 16.8 μW cm^{-1} K^{-2} at 673 K.

Room-temperature Hall measurement was conducted to further clarify the transport mechanism of the carrier. Figure S5 shows that the carrier concentration (n_H) decreases from 1.9 × 10^{19} cm^{-3} to 1.3 × 10^{19} cm^{-3} with increased doping content. It indicates that Ag atoms may become substitutional solutes on the Mg site, resulting in the reduction of n_H. This is interesting, since it is quite different compared to the isoelectronic and same group element Cu addition which did not have such an effect on the carrier concentration, rather showing a slight increase due to interstitial doping[10,29]. Due to the reduced n_H, a large increase in Hall mobility (μ_H) according to the equation $\sigma = ne\mu$ (Figure S5). Weighted mobility (μ_w) is also calculated from the model proposed by Synder[39,40]. The formula is shown below:

$$\mu_w = \frac{3h^3\sigma}{8\pi e(2m_e k_B T)^{\frac{3}{2}}}\left[\frac{\exp\left[\frac{|S|}{k_B/e} - 2\right]}{1+\exp\left[-5(\frac{|S|}{k_B/e}-1)\right]} + \frac{\frac{3}{\pi^2}\frac{|S|}{k_B/e}}{1+\exp\left[5(\frac{|S|}{k_B/e}-1)\right]}\right]$$

In this equation, *h* is the Plank's constant, *e* is the electron charge, m_e is the electron mass and k_B is the Boltzmann's constant. The μ_w is calculated from the measured *S* and σ, which is shown in Figure 3d. With the temperature increasing, μ_w shows a monotonic decrease owing to the acoustic phonon scattering ($\sim T^{-3/2}$) with additional contribution from excited optical phonons[34]. After Ag doping, the sample (x = 0.01) shows a noteworthy enhancement compared with the pristine sample. At 323 K, μ_w raises from 120 cm^2 V^{-1} s^{-1} to 150 cm^2 V^{-1} s^{-1}. As we mentioned before, part of Ag may react with Mg, which leading the suppression of Mg evaporation, and the *in-situ* located at the grain boundary, which is most likely attributed to the higher mobility in the Ag-doped samples. Mostly, the decreased n_H will lead to a higher value of *S*. However, in this work, the trend of the *S* is not consistent with n_H for samples with Ag doping. The *S* as a function of n_H at room temperature based on the single parabolic band model (SPB) is shown in Figure S5. The density of state effective mass (m^*) of the Ag-free sample is approximately 1.0 m_e. As the Ag content increases, the m^* of doped

samples deviates from this value, resulting in minimal changes in the S despite significant changes in the n_H. Also, the decrease on m^* will lead to the fall of μ_w on the x = 0.02 sample since the weighted mobility μ_w is related to the drift mobility μ by $\mu_w = \mu\ (m^*/m_e)^{3/2}$[39]. The reduced m^* will lead to the value of μ_w reduced even if μ monotonously increases (Figure S5).

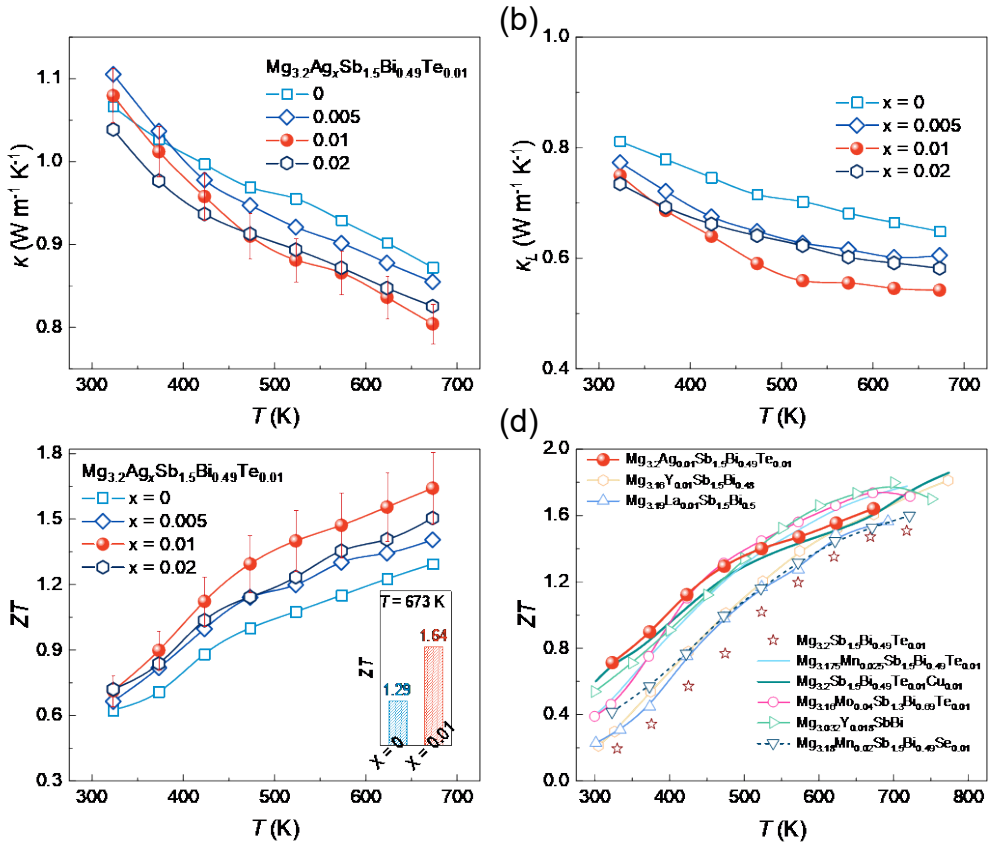

Figure 4. Temperature-dependent (a) κ, (b) κ_L, (cc) ZT of $Mg_{3.2}Ag_xSb_{1.5}Bi_{0.49}Te_{0.01}$ (x = 0, 0.005, 0.01, and 0.02), (d) Comparison of maximum ZT value and average ZT with the state-of-the-art n-type Mg_3Sb_2-based thermoelectrical materials, including $Mg_{3.2}Sb_{1.5}Bi_{0.49}Te_{0.01}$[33], $Mg_{3.2}Sb_{1.5}Bi_{0.49}Te_{0.01}Cu_{0.01}$[10], $Mg_{3.16}Y_{0.01}Sb_{1.5}Bi_{0.48}$[41], $Mg_{3.19}La_{0.01}Sb_{1.5}Bi_{0.5}$[42], $Mg_{3.175}Mn_{0.025}Sb_{1.5}Bi_{0.49}Te_{0.01}$[27], $Mg_{3.16}Mo_{0.04}Sb_{1.3}Bi_{0.69}Te_{0.01}$[43], $Mg_{3.082}Y_{0.018}SbBi$[44], $Mg_{3.18}Mn_{0.02}Sb_{1.5}Bi_{0.49}Se_{0.01}$[45].

The total thermal conductivity κ was calculated by $\kappa = DdC_p$. Before we intended to apply the Dulong-Petit heat capacity (C_v) as the heat capacity (C_p) of materials while calculating the value of κ. Nevertheless, this estimation may lead to a 10% fluctuation in ZT at high temperatures[46]. In this work, we adapted a single polynomial equation proposed by Agne *et al*[46]. As shown in Figure S6, the fitting curve is well corresponded with the LFA results at a high temperature range (over 500 K) compared with the Dulong-Petit method. The results of κ given in Figure 4a, with Ag doping, κ was

decreased from 0.9 W m^{-1} K^{-1} (x = 0) to 0.8 W m^{-1} K^{-1} (x = 0.01) at 673 K. The decreased κ reveals that Ag doping may not only influence the carrier transport but also affect phonons. Therefore, the κ_L and the κ_e were calculated to better understand the phonon transport. In Figure 4b, all doped samples realized a drop in κ_L compared with the pristine sample. One reasonable explanation is that part of Ag occupied the Mg sites leading to an enhancement in phonon scattering, therefore, resulting in a decrease in mean free path and a decrease in κ_L [10,47]. Eventually, we realized a reduction of κ_L from 0.65 W m^{-1} K^{-1} (x = 0) to 0.54 W m^{-1} K^{-1} (x = 0.01) at 673 K. Based on the Wiedemann-Franz law, which is $\kappa_e = L\sigma T$, indicating a positive co-relationship between the κ_e and σ. The merit of κ_e increased naturally from 0.22 W m^{-1} K^{-1} (x = 0.01) to 0.26 W m^{-1} K^{-1} (x = 0) owing to the optimized σ (Figure S7). However, the value of the increase in κ_e is less than the decrease in κ_L, making the total thermal conductivity realized reduced eventually.

The figure of merit ZT was significantly increased during the whole measured temperature range owing to PF and κ optimized simultaneously by Ag doping, as shown in Figure 4c. At 673 K, the $Mg_{3.2}Ag_{0.01}Sb_{1.5}Bi_{0.49}Te_{0.01}$ sample exhibits the highest ZT value, 1.64, realizing great progress on the TE property of Mg_3Sb_2-based in the high-temperature range compared with the 1.29 ZT value of Ag-free doped sample. Furthermore, $(ZT)_{avg}$ is also calculated to compare all the sample TE performance more accurately using the following formula:

$$(ZT)_{avg} = \frac{1}{T_h - T_c}\int_{Tc}^{Th} ZT(T)dT$$

From 323K to 673K, the $Mg_{3.2}Ag_{0.01}Sb_{1.5}Bi_{0.49}Te_{0.01}$ shows $(ZT)_{avg}$ value of 1.27 in comparison with 1.00 for the pristine sample (Figure S8). In Figure 4d, compared to some state-of-the-art Mg_3Sb_2-based TE materials, $Mg_{3.2}Ag_{0.01}Sb_{1.5}Bi_{0.49}Te_{0.01}$ shows high potential for power generation considering the high $(ZT)_{avg}$.

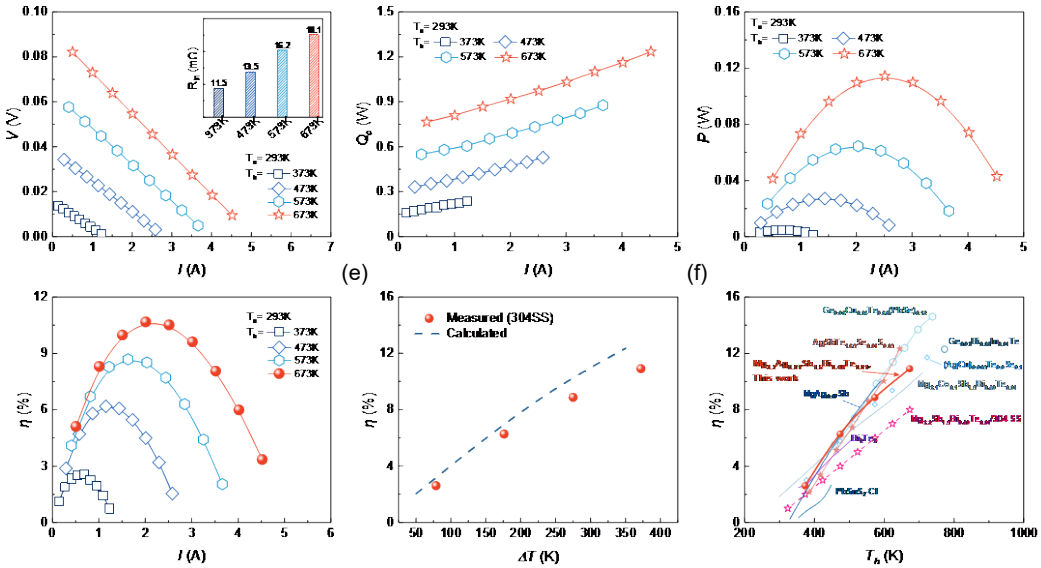

Figure 5. Measured (a) V, (b) P, (c) Q_c, and (d) η of the $Mg_{3.2}Ag_{0.01}Sb_{1.5}Bi_{0.49}Te_{0.01}$-based single thermoelectric element as a function of electrical current (I). The cold-side temperature T_c was maintained at 293 K and the hot-side temperature T_h was set as 373 K, 473 K, 573 K, 673 K, respectively. (e) calculated and practical η_{max} of $Mg_{3.2}Ag_{0.01}Sb_{1.5}Bi_{0.49}Te_{0.01}$ single leg as a function of the temperature difference between hot side and cold side, (f) comparison of η_{max} value of single-leg with $Mg_{3.2}Sb_{1.5}Bi_{0.49}Te_{0.01}$/304 stainless steel[48], $(Ge_{0.98}Cu_{0.04}Te)_{0.88}(PbSe)_{0.12}$[17], $MgAg_{0.97}Sb$[49], $Mg_{3.1}Co_{0.1}Sb_{1.5}Bi_{0.49}Te_{0.01}$[50], $Ge_{0.93}Bi_{0.06}In_{0.01}Te$[18], $(AgCu)_{0.995}Te_{0.9}Se_{0.1}$[51], $AgSbTe_{1.85}Se_{0.01}S_{0.05}$[15], Bi_2Te_3[41] and $PbSnS_2$-Cl[52].

To check the actual TE performance of the $Mg_{3.2}Ag_{0.01}Sb_{1.5}Bi_{0.49}Te_{0.01}$ sample, we fabricated an actual TE single leg based on this material (Figure S9) and tested the conversion efficiency by mini-PEM (Figure S10). The 304 stainless steel (304SS) powder was chosen as the interface material for suppressing interface reaction and contact resistivity[48]. The SEM-EDS measurement was carried out to check the composition and interface of the module. In Figure S11, the interface of 304SS/ $Mg_{3.2}Ag_{0.01}Sb_{1.5}Bi_{0.49}Te_{0.01}$/304SS can be observed clearly, and only a few elements of diffusion across the interfacial layer can be observed, which shows good thermal stability of this single TE element. The contact resistivity is about 16.58 μΩ cm^2, as shown in Figure S12. The power generation characteristics of TE single leg are measured by mini-PEM. Figure 5a-d exhibits the terminal voltage (V), output power (P), output heat flow from the cold side (Q_c), and conversion efficiency (η) of the $Mg_{3.2}Ag_{0.01}Sb_{1.5}Bi_{0.49}Te_{0.01}$-based single thermoelectric element as a function of electrical current (I), respectively. The internal resistance (R_{in}) was obtained according to the slopes of the V-I plots. The value of internal resistance increased from 11.64 mΩ to 18.24 mΩ with

hot-side temperature increasing (Figure 5a). Also, the open-circuit voltage (V_{oc}), which is the *y*-intercept of the *V-I* plot, increases from 15.6 mV at T_h of 373 K to 91.2 mV at T_h of 673 K. Figure 5b shows the *P* as a function of *I*. The maximum value of *P* (= *VI*) increases from 5.23 mW at T_h of 373 K to 113.54 mW at T_h of 673 K under the matched impedance. Q_c increases with the current because of Peltier heating and Joule heating (Figure 5c). Finally, the η was obtained using the following equation: $\eta = P/(P + Q_c)$, as shown in Figure 5d. At 373 K on the hot side, the $\eta_{\max}$ is about 2.58% and reaches 10.67% at 673 K. The theoretical efficiency was also calculated to compare the efficiency gap between the calculation and the measurement result according to the following equation[53]:

$$\eta_{max} = \eta_c \frac{\sqrt{1 + (ZT)_{eng}(\hat{\alpha}/\eta_c - 1/2)} - 1}{\hat{\alpha}(\sqrt{1 + (ZT)_{eng}(\hat{\alpha}/\eta_c - 1/2)} + 1) - \eta_c}$$

In the above equations, η_c is the Carnot efficiency, and $\hat{\alpha}$ is a dmensionless intensity factor of the Thomson effect defined as $\hat{\alpha} = S(T_h)\Delta T / \int_{T_c}^{T_h} S(T)\, dT$. $(ZT)_{eng}$ is the engineering dimensionless figure of merit and can be derived by[53]:

$$(ZT)_{eng} = Z_{eng}\Delta T = \frac{(\int_{T_c}^{T_h} S(T)dT)^2}{\int_{T_c}^{T_h} \rho(T)dT \int_{T_c}^{T_h} \kappa(T)dT}\Delta T = \frac{(PF)_{eng}}{\int_{T_c}^{T_h} \kappa(T)dT}\Delta T$$

$(PF)_{eng}$ is the engineering power factor, T_h and T_c hot-side, and cold-side temperature, respectively. The result of the efficiency calculated and measured is shown in Figure 5e, the maximum calculated efficiency reaches 12.35% at 673 K. Therefore, it can be concluded that the practical conversion efficiency is close to the calculation result. The single leg using 304SS as the contact layer exhibits a high conversion efficiency, owing to the lower contact resistivity and closer coefficient of thermal expansion with TE material[48]. Also, compared with other former works listed in Figure 5f, the fundamental role of Ag in TE performance enhancement can be further confirmed. As a result, 304SS/$Mg_{3.2}Ag_{0.01}Sb_{1.5}Bi_{0.49}Te_{0.01}$/304SS single leg shows a competitive performance, in contrast with other reported single-leg efficiency in different TE material systems. Especially in the low-temperature range (323K), it even has a comparable efficiency with Bi_2Te_3.

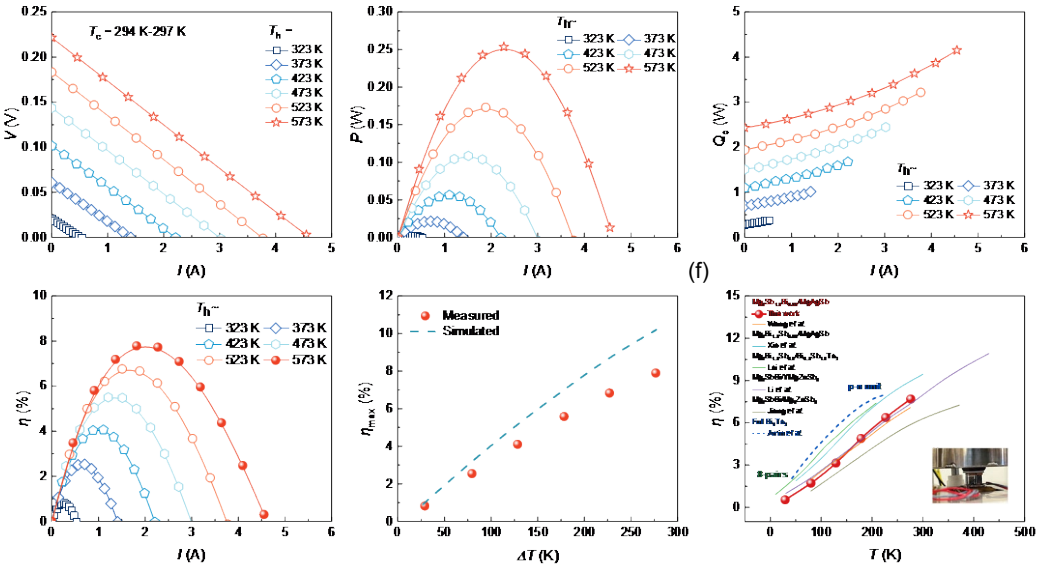

Figure 6. Measured (a) V, (b) P, (c) Q_c, and (d) η of the two-pair 304SS/$Mg_{3.2}Ag_{0.01}Sb_{1.5}Bi_{0.49}Te_{0.01}$/304SS (n-type) and Ag/$Mg_{0.99}Cu_{0.01}Ag_{0.97}Sb_{0.99}$/Ag (p-type) module as a function of electrical current (I). The cold-side temperature T_c was maintained between 294 K – 297 K, whereas the hot-side (T_h) temperature varied from 323 K to 573 K. (e) calculated and practical η_{max} of two-pair module as a function of the temperature difference between hot side and cold side. (f) comparison of η_{max} value of former reported works with our work.

To evaluate the thermoelectric power generation in a further step, we also fabricated the 2-pair TE device comprising an n-type 304SS/$Mg_{3.2}Ag_{0.01}Sb_{1.5}Bi_{0.49}Te_{0.01}$/304SS developed in this work, and the counterpart p-type Ag/$Mg_{0.99}Cu_{0.01}Ag_{0.97}Sb_{0.99}$/Ag [10]. The reason we chose the MgAgSb-based material as p-type material for the module is that $Mg_{0.99}Cu_{0.01}Ag_{0.97}Sb_{0.99}$ can possess a high ZT and ZT_{avg} over 300 K to 600 K (Figure S13). Figure 6a-d shows the measured V, P, Q_c, and the η of the two-pair 304SS/$Mg_{3.2}Ag_{0.01}Sb_{1.5}Bi_{0.49}Te_{0.01}$/304SS (n-type) and Ag/$Mg_{0.99}Cu_{0.01}Ag_{0.97}Sb_{0.99}$/Ag as a (p-type) module as a function of electrical current (I). The cold-side temperature T_c was maintained between 294 K – 297 K, whereas the T_h varied from 323 K to 573 K. The V_{oc} value increases from 21 mV at ΔT of 29 K to 221 mV at ΔT of 277 K, which is in good agreement with simulated values (Figure S14c). The maximum output power (P_{max}) value increases from 2.8 mW at ΔT of 29 K to 253 mW at ΔT of 277 K. The measured P_{max} values are lower than the simulated P_{max} (Figure S14d), mainly attributed to the larger internal resistance (Rin) compared to the measured R_{in}. For example, The R_{in} ~ 48 mΩ is larger than the simulated R_{in} ~ 34 mΩ at ΔT of 277 K (Figure S14e). The difference in the R_{in} between the measured and simulated values is due to the larger contact resistance at the materials interfaces of both n-type and

p-type TE legs. The Q_c value increases from 0.29 W at ΔT of 29 K to 2.43 W at ΔT of 277 K, which is matching with the simulated values (Figure S14f). A η_{max} of ~7.9% is obtained at ΔT of 277 K for the 2-pair module (Figure 6e), which is comparable to the best reported Mg-Sb-based TE modules[54]. Also, it shows a comparable performance and potential with other Mg-based modules and Bi_2Te_3-based units (Figure 6f)[36,55–59] However, the measured η_{max} of ~7.9% is lower than the simulated η_{max} of ~10.2% (Figure 6e). The lower η_{max} is mainly caused by the low P_{max}, which can be further improved by the optimization of the module's interfacial contact resistances.

3. Conclusion

In summary, a promising n-type Mg_3Sb_2-based TE material with a high *ZT* was successfully synthesized by the one-step ball milling and spark plasma sintering method. Ag was found to be an effective dopant for the $Mg_{3.2}Sb_{1.5}Bi_{0.49}Te_{0.01}$ system, with different doping effects compared to the isoelectronic and same group element Cu addition. Whereas, Cu was previously indicated to mainly enter interstitial sites and grain boundaries, in our work we observe that part of Ag atoms may become substitutional solutes on the Mg site. A peak *ZT* value of 1.64 at 673K was achieved for $Mg_{3.2}Ag_{0.01}Sb_{1.5}Bi_{0.49}Te_{0.01}$ which is attributed to the high power factor and low lattice thermal conductivity. With these two effects working simultaneously via Ag doping, we obtained a high TE performance based on the $Mg_{3.2}Sb_{1.5}Bi_{0.49}Te_{0.01}$ system. Moreover, the sandwich-structure TE single leg was also fabricated and exhibited a high conversion efficiency of ~ 10.7% with a hot-side temperature of 673K, which is close to the theoretical result, exhibiting a high potential for medium-temperature thermal energy recycling. Moreover, a 2-pair module fabricated from n-type 304SS/ $Mg_{3.2}Ag_{0.01}Sb_{1.5}Bi_{0.49}Te_{0.01}$/304SS and the p-type Ag/ $Mg_{0.99}Cu_{0.01}Ag_{0.97}Sb_{0.99}$/Ag resulted in high a η_{max} of ~7.9% at ΔT of 277 K.

4. Experimental Section

4.1. Materials preparation

High purity of Mg turnings (99.95%, Sigma Aldrich), Sb grains (99.999%, 5N plus), Bi grains (99.95%, Sigma Aldrich), Te grains (99.95%, Sigma Aldrich), and Ag beads (≥99.99%, Sigma Aldrich) were weighed according to nominal composition ($Mg_{3.2}Ag_xSb_{1.5}Bi_{0.49}Te_{0.01}$, x=0, 0.005, 0.01, and 0.02) in a glovebox with both oxygen and water level less than 1 ppm. Then all the raw materials were loaded into a stainless-steel jar that contained two big balls (diameter is 12.5 mm) in the glove box and ball milled by a high-energy ball mill machine for 5 hours. Then the well-blended powder (2 grams each time) from the ball milling was transferred into a graphite die with an inner diameter of 10 millimeters and immediately sintered by spark plasma sintering (SPS, SPS-1080 System, SPS SYNTEX INC) at sintering temperature 973 K with pressure of 60 MPa for 10 minutes to get the high-density disk samples.

4.2. Phase and microstructure characterizations

The phase structure characterization of sintered disk samples was carried out by X-ray diffraction (XRD, SmartLab3, Rigaku), using Cu Kα radiation with wavelength λ ≈ 1.5406 Å and rotating powder 2θ diffractometer ranging from 10 to 80 degrees. Microstructure and composition analysis of the productions after SPS were tested by field emission scanning electron microscopy (FESEM, Hitachi S-4800 & SU8000) and energy dispersive spectroscopy (EDS) attached to the FESEM equipment.

4.3. Material property characterizations

Bar samples cut from the pressed disks were used for electrical resistivity (ρ) and Seebeck coefficient (S) measurement via a commercial system (ULVAC ZEM-2). The PF (Power Factor) was calculated based on the formula $PF=S^2/\rho$. Total thermal conductivity κ was obtained according to $\kappa=DdC_p$, where D is thermal diffusivity, d is the sample density and C_p is the heat capacity at constant pressure. The density d of samples was confirmed by the Archimedes method, the value of density can be checked in Table S2 and the relative densities of all samples reach ~ 96%. Thermal diffusivity D and heat capacity C_p of the disk sample were measured simultaneously by a laser flash system (Netzsch LFA 467, Germany). Heat capacity C_p was also revised by the polynomial equation

proposed by Agne et al.[46] Electronic thermal conductivity κ_e was calculated by Wiedemann-Franz law: $\kappa_e = L\sigma T$, where L is Lorenz number, which can be expressed by the equation: $L = 1.5 + exp\ [-|S|/116]$[60]. Lattice thermal conductivity κ_L was obtained by subtracting electronic thermal conductivity from the total thermal conductivity. The measurement uncertainties of commercial instruments for the individual physical properties are 7% for electrical conductivity, 8.5% for power factor, 6% for thermal conductivity, and 11% for zT. The Hall carrier concentration (n_H) was obtained using equation $n_H = 1/eR_H$, where e is the electronic charge and R_H is the Hall coefficient. The room temperature Hall coefficient R_H was measured using PPMS (Physical Properties Measurement System, Quantum Design) with the AC transport option.

4.4. Single-leg and 2-pair module fabrication and characterization

The $Mg_{3.2}Ag_{0.01}Sb_{1.5}Bi_{0.49}Te_{0.01}$ single-leg with 304 stainless-steel contact layers at both ends was prepared by SPS: The ball-milled $Mg_{3.2}Ag_{0.01}Sb_{1.5}Bi_{0.49}Te_{0.01}$ powder was loaded between the stainless-steel powder each side in the graphite die and sintered by SPS using the condition as of the bulk material sintering described before[61]. For the fabrication of a 2-pair module, the $Mg_{0.99}Cu_{0.01}Ag_{0.97}Sb_{0.99}$ TE was used as a counterpart p-type leg. The p-type powder was sandwiched between the Ag powder on each side and sintered by using the same conditions as reported[61]. The obtained sandwich-structure joints were ground, polished, and then cut into bulk with dimensions of ~ 3 × ~3 × ~5.1 mm. The 2-pair module fabrication was similar to the previous report. It was fabricated by positioning the p- and n-type TE lags on the Cu substrate with dimensions of 10 mm A × 10 mm × 0.5 mm, where 0.21 mm thick Cu patterns were printed onto the 0.08 mm thick heat-conducting polymer film. The legs were 7 mm × 3 mm × 1 mm. Liquid In-Ga eutectic alloy was smeared between legs and Cu interconnecting electrodes to reduce the electrical and thermal contact resistances. The conversion efficiency of the single-leg and 2-pair module was measured with hot-side temperatures of 50 °C, 100 °C, 200 °C, 300 °C, 400 °C utilizing a commercial testing apparatus (Mini-PEM, ADVANCE RIKO, Japan)[60]. The cold-side temperature was maintained at 20–25 °C.

Supporting Information

Supporting Information is available from the Wiley Online Library or from the author.

Acknowledgments

This work was supported by JST Mirai Program Grant Number JPMJMI19A1.

Conflict of Interest

The authors declare no conflict of interest.

Author Contributions

J.L. contributed to the sample preparations, characterization, writing, and revising the manuscript. C.R. contributed to the guidance of the experiment, module fabrication, and evaluation and revision of the manuscript. Z.L. contributed to the methodology, experiment guidance, and revision of the manuscript. W.G. contributed to the experiment guidance and revision of the manuscript. T.M. led the project, providing supervision, conceptualization, methodology, writing-review and editing, and funding acquisition. All authors contributed to the review of the final manuscript.

Data Availability

The data that support the findings of this study are included in the article and its supplementary information files and are available from the corresponding author upon reasonable request.

References

[1] T. Mori, S. Priya, *MRS Bull.* **2018**, *43*, 176.
[2] I. Petsagkourakis, K. Tybrandt, X. Crispin, I. Ohkubo, N. Satoh, T. Mori, *Sci. Technol. Adv. Mater.* **2018**, *19*, 836.
[3] T. Hendricks, T. Caillat, T. Mori, *Energies* **2022**, *15*, 7307.
[4] J. He, T. M. Tritt, *Science* **2017**, *357*, eaak9997.
[5] Y. Pei, X. Shi, A. LaLonde, H. Wang, L. Chen, G. J. Snyder, *Nature* **2011**, *473*, 66.
[6] S. Ning, S. Huang, Z. Zhang, N. Qi, M. Jiang, Z. Chen, X. Tang, *J. Materiomics* **2022**, *8*, 1086.
[7] Y. Pei, H. Wang, G. J. Snyder, *Adv. Mater.* **2012**, *24*, 6125.
[8] X. Shi, X. Zhang, A. Ganose, J. Park, C. Sun, Z. Chen, S. Lin, W. Li, A. Jain, Y. Pei, *Mater. Today Phys.* **2021**, *18*, 100362.
[9] J. Mao, Y. Wu, S. Song, Q. Zhu, J. Shuai, Z. Liu, Y. Pei, Z. Ren, *ACS Energy Lett.*

2017, *2*, 2245.
[10] Z. Liu, N. Sato, W. Gao, K. Yubuta, N. Kawamoto, M. Mitome, K. Kurashima, Y. Owada, K. Nagase, C.-H. Lee, J. Yi, K. Tsuchiya, T. Mori, *Joule* **2021**, *5*, 1196.
[11] F. Jiang, T. Feng, Y. Zhu, Z. Han, R. Shu, C. Chen, Y. Zhang, C. Xia, X. Wu, H. Yu, C. Liu, Y. Chen, W. Liu, *Mater. Today Phys.* **2022**, *27*, 100835.
[12] Y. Wang, X. Zhang, Y. Wang, N. Liu, Y. Liu, Q. Lu, *J. Mater. Sci.* **2022**, *57*, 3183.
[13] T. Kanno, H. Tamaki, M. Yoshiya, H. Uchiyama, S. Maki, M. Takata, Y. Miyazaki, *Adv. Funct. Mater.* **2021**, *31*, 2008469.
[14] M. Hong, Z.-G. Chen, J. Zou, *Chin. Phys. B* **2018**, *27*, 048403.
[15] Y. Zhang, Z. Li, S. Singh, A. Nozariasbmarz, W. Li, A. Genç, Y. Xia, L. Zheng, S. H. Lee, S. K. Karan, G. K. Goyal, N. Liu, S. M. Mohan, Z. Mao, A. Cabot, C. Wolverton, B. Poudel, S. Priya, *Adv. Mater.* **n.d.**, *n/a*, 2208994.
[16] V. Taneja, S. Das, K. Dolui, T. Ghosh, A. Bhui, U. Bhat, D. K. Kedia, K. Pal, R. Datta, K. Biswas, *Adv. Mater.* **n.d.**, *36*, 2307058.
[17] Z. Bu, X. Zhang, B. Shan, J. Tang, H. Liu, Z. Chen, S. Lin, W. Li, Y. Pei, *Sci. Adv.* **2021**, *7*, eabf2738.
[18] S. Perumal, M. Samanta, T. Ghosh, U. S. Shenoy, A. K. Bohra, S. Bhattacharya, A. Singh, U. V. Waghmare, K. Biswas, *Joule* **2019**, *3*, 2565.
[19] D. Li, X.-L. Shi, Z. Feng, M. Li, J. Zhu, X. Ma, L. Zhang, H. Zhong, W.-D. Liu, S. Li, Z.-G. Chen, *Adv. Funct. Mater.* **2023**, *33*, 2305269.
[20] J. Wang, M. Guo, J. Zhu, D. Qin, F. Guo, Q. Zhang, W. Cai, J. Sui, *J. Mater. Sci. Technol.* **2020**, *59*, 189.
[21] A. Li, C. Fu, X. Zhao, T. Zhu, *Research* **2020**, *2020*, 2020/1934848.
[22] H. Cho, S. Y. Back, N. Sato, Z. Liu, W. Gao, L. Wang, H. D. Nguyen, N. Kawamoto, T. Mori, *Adv. Funct. Mater.* **n.d.**, *n/a*, 2407017.
[23] Z. Zhou, G. Han, X. Lu, G. Wang, X. Zhou, *J. Magnes. Alloys* **2022**, *10*, 1719.
[24] S. Xiao, K. Peng, Z. Zhou, H. Wang, S. Zheng, X. Lu, G. Han, G. Wang, X. Zhou, *J. Magnes. Alloys* **2023**, *11*, 2486.
[25] C. L. Condron, S. M. Kauzlarich, F. Gascoin, G. J. Snyder, *J. Solid State Chem.* **2006**, *179*, 2252.
[26] H. Tamaki, H. K. Sato, T. Kanno, *Adv. Mater.* **2016**, *28*, 10182.
[27] X. Chen, H. Wu, J. Cui, Y. Xiao, Y. Zhang, J. He, Y. Chen, J. Cao, W. Cai, S. J. Pennycook, Z. Liu, L.-D. Zhao, J. Sui, *Nano Energy* **2018**, *52*, 246.
[28] X. Li, B. Yang, H. Xie, H. Zhong, S. Feng, Y. Zhang, Y. Ma, J. Zhang, H. Su, *Mater. Res. Bull.* **2023**, *159*, 112106.
[29] Z. Liu, W. Gao, H. Oshima, K. Nagase, C.-H. Lee, T. Mori, *Nat. Commun.* **2022**, *13*, 1120.
[30] A. Li, P. Nan, Y. Wang, Z. Gao, S. Zhang, Z. Han, X. Zhao, B. Ge, C. Fu, T. Zhu, *Acta Mater.* **2022**, *239*, 118301.
[31] X. Wu, X. Ma, H. Yao, K. Liang, P. Zhao, S. Hou, L. Yin, H. Yang, J. Sui, X. Lin, F. Cao, Q. Zhang, J. Mao, *ACS Appl. Mater. Interfaces* **2023**, *15*, 50216.
[32] J.-W. Li, Z. Han, J. Yu, H.-L. Zhuang, H. Hu, B. Su, H. Li, Y. Jiang, L. Chen, W. Liu, Q. Zheng, J.-F. Li, *Nat. Commun.* **2023**, *14*, 7428.
[33] T. Kanno, H. Tamaki, H. K. Sato, S. D. Kang, S. Ohno, K. Imasato, J. J. Kuo, G.

J. Snyder, Y. Miyazaki, *Appl. Phys. Lett.* **2018**, *112*, 033903.
[34] M. Wood, J. J. Kuo, K. Imasato, G. J. Snyder, *Adv. Mater.* **2019**, *31*, 1902337.
[35] X. Huang, C. Li, M. Yuan, J. Shuai, X.-G. Li, Y. Hou, *Mater. Today Phys.* **2024**, *43*, 101386.
[36] L. Wang, W. Zhang, S. Y. Back, N. Kawamoto, D. H. Nguyen, T. Mori, *Nat. Commun.* **2024**, *15*, 6800.
[37] S. Terlicka, A. Dębski, A. Sypien, W. Gąsior, A. Budziak, *Mater. Today Commun.* **2021**, *29*, 102946.
[38] C. Hu, K. Xia, C. Fu, X. Zhao, T. Zhu, *Energy Environ. Sci.* **2022**, *15*, 1406.
[39] G. J. Snyder, A. H. Snyder, M. Wood, R. Gurunathan, B. H. Snyder, C. Niu, *Adv. Mater.* **2020**, *32*, 2001537.
[40] G. J. Snyder, A. Pereyra, R. Gurunathan, *Adv. Funct. Mater.* **2022**, *32*, 2112772.
[41] J.-W. Li, W. Liu, W. Xu, H.-L. Zhuang, Z. Han, F. Jiang, P. Zhang, H. Hu, H. Gao, Y. Jiang, B. Cai, J. Pei, B. Su, Q. Li, K. Hayashi, H. Li, Y. Miyazaki, X. Cao, Q. Zheng, J.-F. Li, *Adv. Mater.* **n.d.**, *n/a*, 2209119.
[42] F. Zhang, C. Chen, S. Li, L. Yin, B. Yu, J. Sui, F. Cao, X. Liu, Z. Ren, Q. Zhang, *Adv. Electron. Mater.* **2020**, *6*, 1901391.
[43] L. Wang, N. Sato, Y. Peng, R. Chetty, N. Kawamoto, D. H. Nguyen, T. Mori, *Adv. Energy Mater.* **2023**, *13*, 2301667.
[44] X. Shi, T. Zhao, X. Zhang, C. Sun, Z. Chen, S. Lin, W. Li, H. Gu, Y. Pei, *Adv. Mater.* **2019**, *31*, 1903387.
[45] J. Liang, H. Yang, C. Liu, L. Miao, J. Chen, S. Zhu, Z. Xie, W. Xu, X. Wang, J. Wang, B. Peng, K. Koumoto, *ACS Appl. Mater. Interfaces* **2020**, *12*, 21799.
[46] M. T. Agne, K. Imasato, S. Anand, K. Lee, S. K. Bux, A. Zevalkink, A. J. E. Rettie, D. Y. Chung, M. G. Kanatzidis, G. J. Snyder, *Mater. Today Phys.* **2018**, *6*, 83.
[47] L. Yu, W. Li, Z. Zhang, S. Wei, J. Li, Z. Ji, J. Zhuo, G. Lu, W. Song, *Mater. Today Phys.* **2022**, *26*, 100721.
[48] L. Yin, C. Chen, F. Zhang, X. Li, F. Bai, Z. Zhang, X. Wang, J. Mao, F. Cao, X. Chen, J. Sui, X. Liu, Q. Zhang, *Acta Mater.* **2020**, *198*, 25.
[49] Z. Liu, J. Shuai, J. Mao, Y. Wang, Z. Wang, W. Cai, J. Sui, Z. Ren, *Acta Mater.* **2016**, *102*, 17.
[50] Q. Zhu, S. Song, H. Zhu, Z. Ren, *J. Power Sources* **2019**, *414*, 393.
[51] J. Jiang, H. Zhu, Y. Niu, Q. Zhu, S. Song, T. Zhou, C. Wang, Z. Ren, *J. Mater. Chem. A* **2020**, *8*, 4790.
[52] S. Zhan, T. Hong, B. Qin, Y. Zhu, X. Feng, L. Su, H. Shi, H. Liang, Q. Zhang, X. Gao, Z.-H. Ge, L. Zheng, D. Wang, L.-D. Zhao, *Nat. Commun.* **2022**, *13*, 5937.
[53] H. S. Kim, W. Liu, G. Chen, C.-W. Chu, Z. Ren, *Proc. Natl. Acad. Sci.* **2015**, *112*, 8205.
[54] S. Bano, R. Chetty, J. Babu, T. Mori, *Device* **2024**, *2*, DOI 10.1016/j.device.2024.100408.
[55] J. Lei, K. Zhao, J. Liao, S. Yang, Z. Zhang, T.-R. Wei, P. Qiu, M. Zhu, L. Chen, X. Shi, *Nat. Commun.* **2024**, *15*, 6588.
[56] L. Yin, X. Li, X. Bao, J. Cheng, C. Chen, Z. Zhang, X. Liu, F. Cao, J. Mao, Q. Zhang, *Nat. Commun.* **2024**, *15*, 1468.

[57] M. Jiang, Y. Fu, Q. Zhang, Z. Hu, A. Huang, S. Wang, L. Wang, W. Jiang, *Natl. Sci. Rev.* **2023**, *10*, nwad095.
[58] L. Xie, L. Yin, Y. Yu, G. Peng, S. Song, P. Ying, S. Cai, Y. Sun, W. Shi, H. Wu, N. Qu, F. Guo, W. Cai, H. Wu, Q. Zhang, K. Nielsch, Z. Ren, Z. Liu, J. Sui, *Science* **2023**, *382*, 921.
[59] A. Nozariasbmarz, B. Poudel, W. Li, H. B. Kang, H. Zhu, S. Priya, *iScience* **2020**, *23*, 101340.
[60] H.-S. Kim, Z. M. Gibbs, Y. Tang, H. Wang, G. J. Snyder, *APL Mater.* **2015**, *3*, 041506.
[61] Y. Liu, L. Yin, W. Zhang, J. Wang, S. Hou, Z. Wu, Z. Zhang, C. Chen, X. Li, H. Ji, Q. Zhang, Z. Liu, F. Cao, *Cell Rep. Phys. Sci.* **2021**, *2*, 100412.